Gold Bull (2013) 46:153–159
DOI 10.1007/s13404-013-0092-y

ORIGINAL PAPER

Self-assembled ferrite nanodots on multifunctional Au nanoparticles

Yukiko Yasukawa · Xiaoxi Liu · Akimitsu Morisako

Published online: 29 May 2013

Abstract The fabrication of magnetic oxide nanodots was studied without the use of conventional lithographic techniques and patterning masks. Self-assembled Au nanoparticles with an average size of approximately 17 nm were formed via simple sputtering and used as the underlayer for the magnetic oxide film. Subsequently, hexagonal ferrite, $SrFe_{12}O_{19}$, was sputtered on the Au nanoparticles, resulting in an $SrFe_{12}O_{19}$/Au sample. Self-assembled $SrFe_{12}O_{19}$ nanodots were obtained with an average size of 40–50 nm. The morphology of the Au nanoparticle underlayer acted as a template for the $SrFe_{12}O_{19}$ film, such that the self-assembled $SrFe_{12}O_{19}$ nanodots were formed. In addition, the fabrication of the $SrFe_{12}O_{19}$ film on the Au nanoparticles induced the down-sizing of the magnetic domain structures of $SrFe_{12}O_{19}$ to the nanoscale. Importantly, although the nanodots showed nanometric magnetic domains, a sufficient magnetization magnitude in the $SrFe_{12}O_{19}$ nanodots was revealed. Furthermore, the $SrFe_{12}O_{19}$ nanodot fabrication area was ~8.5 cm^2, thereby the current technique can be applied to the development of future functional magnetic nanodots.

Keywords Sputtering · Self-assembly · Au nanoparticles · Hexaferrite · Magnetic nanodots

Introduction

Processing of magnetic nanostructures is currently crucial in the field of magnetic engineering, such as for magnetic hyperthermia [1], drug delivery systems [2], environmental purification [3], and magnetic recording systems [4]. For instance, with respect to magnetic recording systems, the immediate development of ultrahigh density magnetic recording media is indispensable because of the explosive worldwide increase in digital information. Patterned media [5–7], in which data are stored in a physically isolated single magnetic domain, have the potential for application in ultrahigh-density magnetic recording systems offering magnetic bit areal densities above 2×10^{12} bits/in.. On the basis of these requirements, nanofabrication techniques for magnetic films and subsequent magnetic nanostructures are the latest key topics.

Hexagonal structural ferrite, $SrFe_{12}O_{19}$, is known to exhibit a large anisotropy constant (K_1) value of 3.5×10^6 erg/cm^3 [8] and is widely used as a ferrite magnet. $SrFe_{12}O_{19}$ also shows sufficient chemical stability, corrosion resistance, and superior wear resistance; these characteristics make $SrFe_{12}O_{19}$ suitable for use in functional magnetic nanoparticles. The combined feature of superior wear resistance and a high K_1 value is one of the important factors in the fabrication of magnetic nanostructures. Sufficient magnetic properties can be expected, even after nanofabrication of $SrFe_{12}O_{19}$, due to the large K_1 value, while the wear resistance easily enables fabrication of $SrFe_{12}O_{19}$ at the nanoscale. In spite of these advantages, there are only a few reports on the processing of hexagonal ferrites that are ten to several tens of nanometers in size. Therefore, it is worth studying the fabrication of $SrFe_{12}O_{19}$ on the several tens of nanometers or slightly larger scale to investigate its potential in future applications such as functional magnetic nanodevices.

A wide variety of techniques have been reported for the preparation of magnetic nanostructures, such as imprint lithography [9–11], ion irradiation [12, 13], focused ion beam lithography [14, 15], electron beam lithography [6, 16, 17], and a combination of lithographic techniques and electrochemical deposition of magnetic materials [17]. However, structural and magnetic damage are unavoidable issues in lithography. In addition, the fabrication areas are limited, and many experimental procedures are required when using lithographic-based techniques. On the other hand, nanofabrication based on the self-assembly technique is a promising method for attaining magnetic nanostructures, because this approach involves

Y. Yasukawa (✉) · X. Liu · A. Morisako
Department of Computer Science and Engineering, Faculty of Engineering, Shinshu University, 4-17-1 Wakasato, Nagano 380-8553, Japan
e-mail: yasukawa@shinshu-u.ac.jp

inexpensive equipment, simple procedures, large fabrication areas, and there is no need for patterning masks. Furthermore, structural and magnetic damage does not occur. In fact, nanofabrication of magnetic films using the self-assembly technique has recently been widely reported [18, 19].

In this study, $SrFe_{12}O_{19}$ was selected as the target material. $SrFe_{12}O_{19}$ exhibits perpendicular magnetic anisotropy when the $SrFe_{12}O_{19}$ (00*l*) planes are stacked along the *c*-axis direction. The lattice parameter, *a*, of $SrFe_{12}O_{19}$ is 5.89 Å (JCPDS card; 33–1340). Meanwhile, the interatomic distance, *d*, of Au (111) calculated based on the JCPDS card (04–0784) is 5.77 Å. Because the misfit ratio between *a*[$SrFe_{12}O_{19}$ (00*l*)] and *d*[Au(111)] is ~2.1 %, heteroepitaxial growth between $SrFe_{12}O_{19}$ (00*l*) and Au (111) could be expected. In fact, $SrFe_{12}O_{19}$ (00*l*) was successfully grown on Au (111) and its magnetic properties were studied in our previous works [20–23]. However, the physical sources for magnetic properties, e. g., magnetic domain structures and nanometric crystal structures of the $SrFe_{12}O_{19}$ (00*l*)/Au (111) samples, were not studied in detail.

On the basis of these backgrounds, the structuring of $SrFe_{12}O_{19}$ nanodots was studied using the self-assembly technique. First, fabrication of self-assembled Au nanoparticles on a substrate was achieved via sputtering. These Au nanoparticles were then used as an underlayer for the $SrFe_{12}O_{19}$ film. The Au nanoparticle underlayer was utilized to downsize the $SrFe_{12}O_{19}$ film in order to form $SrFe_{12}O_{19}$ nanodot structures because the morphology of the upper layer ($SrFe_{12}O_{19}$) must reflect the structure of the underlayer (self-assembled Au nanoparticles). The nanostructures of the $SrFe_{12}O_{19}$/Au samples were carefully observed, and correlations between the $SrFe_{12}O_{19}$ nanostructures and the macroscopic magnetic properties of $SrFe_{12}O_{19}$ in the $SrFe_{12}O_{19}$/Au samples were also discussed.

Experimental

Samples were prepared on a SiO_2/Si substrate using a DC magnetron sputtering system of our own making. The vacuum chamber of sputtering machine was evacuated to reach the pressure of $0.8–1.4\times10^{-6}$ Torr. In order to form the self-assembled Au nanoparticles, Au sputtering was performed in an Ar atmosphere at a sputtering pressure of 2.0×10^{-3} Torr with a deposition power density of ~0.49 W/cm^2 for 1 min at a substrate temperature (T_S) of 100 °C. Subsequently, $SrFe_{12}O_{19}$ was deposited by DC magnetron sputtering on Au in a mixture of Ar and O_2 gasses at a fixed partial-pressure ratio of P_{Ar}: P_{O2}=99:1. The $SrFe_{12}O_{19}$ sputtering was carried out at sputtering pressure of 2.0×10^{-3} Torr with ~0.99 W/cm^2 for 1 h at a T_S of 475 °C using a sintered off-stoichiometric ceramic target ($SrFe_{11}O_x$, ϕ 50.8 mm with a thickness of 5 mm; Kojundo Chemical Laboratory). The crystallization of $SrFe_{12}O_{19}$ could be possible at T_S=475 °C, but it should be noted that this temperature is close to the lowest limit for the crystallization of $SrFe_{12}O_{19}$ [20, 22]. Therefore, a post-annealing was carried out for the sufficient crystallization of $SrFe_{12}O_{19}$. The sample was annealed in a furnace under an air atmosphere at 750 °C for 1 h after $SrFe_{12}O_{19}$ deposition.

An X-ray diffractometer (XRD; Rigaku SmartLab) was used to identify the obtained material phases. The local nanostructures of the samples were studied using field-emission scanning electron microscopy (FE-SEM; Hitachi SU8000) and transmission electron microscopy (TEM; JEOL JEM-2010). Atomic force microscopy (AFM; Veeco Innova) was used to acquire the morphologies of the samples. The magnetic domains and magnetic properties were evaluated by magnetic force microscopy (MFM; Veeco Innova) and vibrating sample magnetometer (VSM; Tamagawa Factory Co. Ltd. custom made), respectively, at room temperature.

Results and discussion

It was possible to control the morphology of Au and change it from a film (Fig. 1a) to self-assembled nanoparticles (Fig. 1b) using an in situ heat treatment of the substrate at 100 °C during sputtering. The total energy (E_{total}) of this system can be classified into (1) the surface energy (γ) of the Au film, (2) the interfacial energy between the substrate and the Au film, (3) the γ of the substrate, and (4) the elastic strain energy of the Au film. Energies (1) and (3) originate from the surface curvatures, whereas (2) is generated by the wettability of the Au and the substrate. Furthermore, the misfit between the Au film and the substrate induces (4). The summation of (1)–(4) generates E_{total} in this system. Through in situ heating of the substrate during the sputtering, the Au adatoms diffuse on the substrate. The driving force for the formation of the Au nanoparticles from the Au film is a reduction of E_{total} by altering the morphology of Au. Consequently, Au nanoparticles were obtained. Figure 1c shows the XRD pattern for the self-assembled nanoparticles (Fig. 1b). It was found that Au exhibits a (111) orientation. The γ of *fcc* structural metals including Au is known to be $\gamma(111)<\gamma(100)<\gamma(110)$ in general [24]. Therefore, Au is oriented toward the direction of the lowest γ, (111). The diameter (size) and distribution of the Au nanoparticles shown in Fig. 1b were evaluated by SEM as summarized in Fig. 1d. The average size of the self-assembled Au nanoparticles was approximately 17 nm with a standard deviation value of ~7.6. It was reported that the size of Au nanoparticles was 32 nm under the close experimental parameters to the current study [22]. We achieved finer and more homogeneous size of Au nanoparticles in the current case. The areal density of Au nanoparticles calculated from SEM image was $\sim1.2\times10^{12}$ particles/in., which is

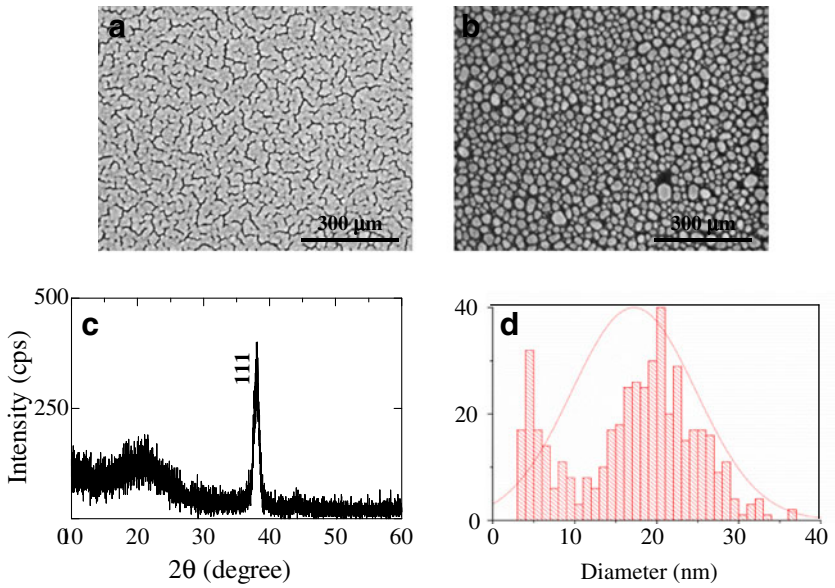

Fig. 1 Top view SEM images of **a** initial Au film and **b** self-assembled Au nanoparticles. The sputtering time for both samples was 1 min. **c** XRD diagram of **b**. **d** Histogram of Au nanoparticle size in **b**

close to the density required for the future ultrahigh density magnetic recording media.

Figure 2a–h show cross-sectional TEM images of the Au nanoparticles (Fig. 2a and b), $SrFe_{12}O_{19}$ (Fig. 2e and f), and $SrFe_{12}O_{19}$/Au (Fig. 2c, d, g, and h). Figure 2b, d, f, and h are high magnification images of Fig. 2a, c, e, and g, respectively. Completely isolated, island-like elliptical Au nanoparticles were obtained (Fig. 2a and b). The height of the nanodots was ~10 nm, which is the same as the thickness of the original Au film (Fig. 1a) as revealed in the TEM cross-sectional observations (data not shown). For the $SrFe_{12}O_{19}$/Au sample (Fig. 2c and d), lattice fringes on the Au nanoparticles were observed (Fig. 2d). It is reasonable to consider that the lattice fringes originate from crystalline $SrFe_{12}O_{19}$, such that the crystallization of $SrFe_{12}O_{19}$ would be accelerated on the Au nanoparticles. Figure 2e and f show $SrFe_{12}O_{19}$ prepared directly on the substrate with subsequent post-annealing at 750 °C for 1 h in air without the Au underlayer. Well-oriented lattice fringes of $SrFe_{12}O_{19}$ are observed, but note the creation of a ~7.2-nm thick amorphous layer between the crystalline $SrFe_{12}O_{19}$ and SiO_2 layers indicated by the arrows (Fig. 2f). This amorphous phase may be due to an interdiffusion layer consisting of $SrFe_{12}O_{19}$ and the substrate—namely, a mixture of Sr, Fe, Si, and O. Figure 2g and h show $SrFe_{12}O_{19}$/Au after post annealing of the samples shown in Fig. 2c and d, respectively, at 750 °C for 1 h in air. Similar to the case of Fig. 2d, the lattice fringes of $SrFe_{12}O_{19}$ were observed on the Au nanoparticle (Fig. 2h).

To gain detailed information on the creation of the crystalline $SrFe_{12}O_{19}$ nanodots using the present fabrication technique, Fourier transformations of the obtained TEM image (Fig. 3a) for the $SrFe_{12}O_{19}$/Au sample were carried out (Fig. 3b–g). The sample was similar to those of Fig. 2c and d. The transformed areas are indicated as rectangles in Fig. 3a. No diffraction spots were observed in Fig. 3b, d, and g, whereas spots were seen in Fig. 3c and f. These Fourier transformed spots suggest the existence of crystalline $SrFe_{12}O_{19}$. By comparing Fig. 3a, c, and f, the lattice fringes of $SrFe_{12}O_{19}$ were determined to be created on the

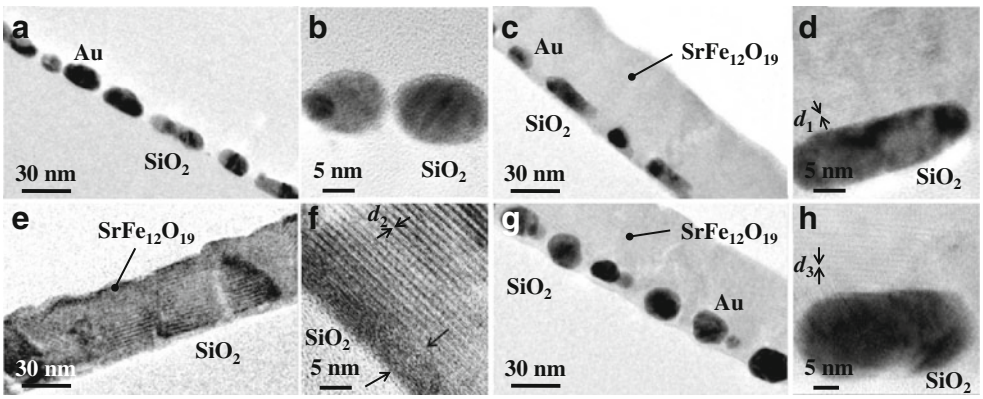

Fig. 2 Cross-sectional TEM images for **a** Au nanoparticles corresponding to those in Fig. 1b and **b** enlarged image. **c** and **d** $SrFe_{12}O_{19}$ deposited on the Au nanoparticles at T_S=475 °C. **e** $SrFe_{12}O_{19}$ prepared directly on the substrate at T_S=475 °C with post annealing at 750 °C for 1 h in air. **f** Magnified image of **e**. **g** and **h** Effects of post annealing on samples **c** and **d** at 750 °C for 1 h in air

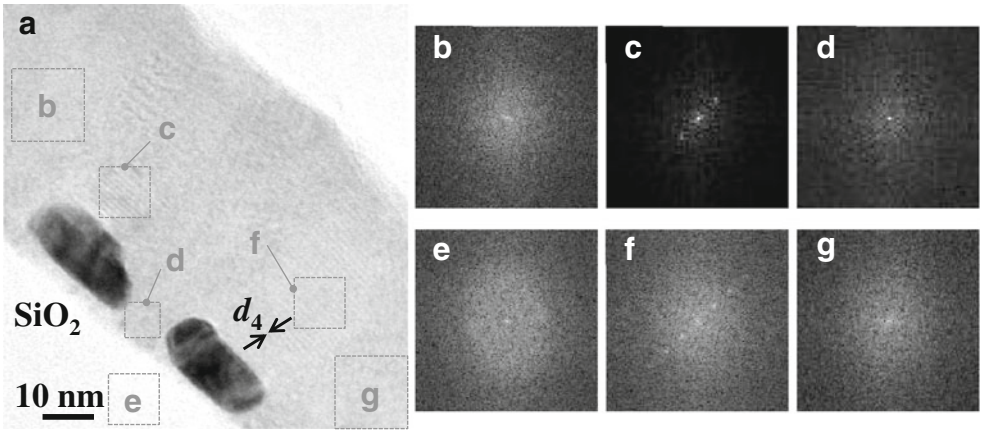

Fig. 3 **a** Cross-sectional TEM and **b**–**g** local Fourier transformation images of $SrFe_{12}O_{19}$ on Au nanoparticles prepared at T_S=475 °C. **b**, **d**, and **g** Transformed images of $SrFe_{12}O_{19}$ at the interspaces of the Au nanoparticles. **c** and **f** Fourier transformed images of $SrFe_{12}O_{19}$ on the Au nanoparticles. **e** Transformed image of the SiO_2/Si substrate. Transformed areas are indicated as *rectangles*

Au nanoparticles. On the other hand, the amorphous Sr–Fe–O seen in Fig. 3b, d, and g corresponds to the interspaces of the Au nanoparticles, i.e., the SiO_2 substrate portions. From these results, it was concluded that the crystalline $SrFe_{12}O_{19}$ formed preferentially on the Au nanoparticles rather than on the SiO_2 substrate. Promotion of $SrFe_{12}O_{19}$ crystallization on the Au nanoparticles is probably due to the relatively lower crystallization temperature of $SrFe_{12}O_{19}$ on Au than that on SiO_2. The coexistence of the crystalline $SrFe_{12}O_{19}$ and amorphous Sr–Fe–O sections in the same $SrFe_{12}O_{19}$/Au phase was then experimentally clarified. Figure 3e shows the Fourier-transformed image of the SiO_2 substrate area. Because SiO_2 is amorphous, no diffraction spots were observed, and the result is thus similar to those seen in Fig. 3b, d, and g.

Notably, the local nanostructures discussed above were well reflected in the macroscopic crystal structures of $SrFe_{12}O_{19}$. Single-phase $SrFe_{12}O_{19}$ can be seen in Fig. 4a, which shows the diffraction lines from the (00*l*) planes except the (107) plane, which is the strongest in the $SrFe_{12}O_{19}$ powder system. In Fig. 4b, the preferential (00*l*) orientation of $SrFe_{12}O_{19}$ coincident with the Au (111) orientation was indexed. The XRD measurements indicated that the Au nanoparticle underlayers enhanced the (00*l*) orientation of $SrFe_{12}O_{19}$. Taking into account the present XRD results, it is reasonable to denote the spacing of the

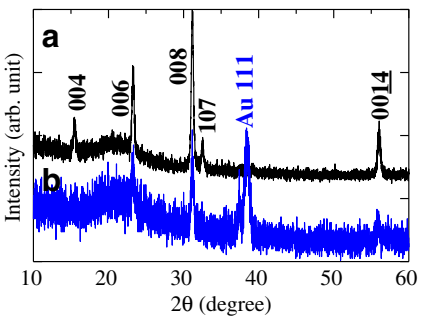

Fig. 4 XRD patterns of **a** $SrFe_{12}O_{19}$ and **b** $SrFe_{12}O_{19}$/Au samples. Both samples are the same as those shown in Fig. 2e and f and Fig. 2g and h, respectively

lattice planes (d_1–d_4) indicated in Figs. 2d (d_1), 2f (d_2), 2h (d_3), and 3a (d_4) as $SrFe_{12}O_{19}$ (00*l*) planes and/or the (107) plane. We estimated the d_1–d_4 values from TEM images, and the representative $SrFe_{12}O_{19}$ plane for each *d* value was determined. The experimentally obtained *d* values (d_1–d_4) and those reported in the JCPDS card (No. 33–1340) were then compared. The differences (Δ) between the experimentally determined *d* values and those of the JCPDS card were evaluated as $(d_{experiment}-d_{JCPDS})/d_{JCPDS}\times 100$. The results are tabulated (Table 1). For the $SrFe_{12}O_{19}$/Au samples (d_1, d_3, and d_4), the (004) and (008) planes were indexed, suggesting that the Au underlayers promoted the (00*l*) orientation of $SrFe_{12}O_{19}$, which is essential for the perpendicular magnetic anisotropy of $SrFe_{12}O_{19}$. Meanwhile, the (107) plane was identified from the d_2 value for the $SrFe_{12}O_{19}$ sample without the Au underlayer. The $SrFe_{12}O_{19}$ (107) component deteriorates the perpendicular magnetic anisotropy of the overall $SrFe_{12}O_{19}$.

Figure 5a and d, respectively, show the surface morphologies of the $SrFe_{12}O_{19}$ and $SrFe_{12}O_{19}$/Au samples. The samples seen in Fig. 5a–c and d–f are the same as those shown in Figs. 2e, f, and 4a and Figs. 2g, h, and 4b, respectively. For the $SrFe_{12}O_{19}$ monolayer, the surface roughness is large and exhibits abnormal growth of grains, which are indicated by the highlighted contrasts in the image. In the meantime, Fig. 5d shows the self-assembled $SrFe_{12}O_{19}$ nanodot structures. The estimated size of the $SrFe_{12}O_{19}$ nanodots was found to be 40–50 nm. The

Table 1 Calculated *d* values based on the TEM observations and corresponding $SrFe_{12}O_{19}$ crystallographic planes. Reported *d* values from the JCPDS card are also listed. Δ represents the difference in the experimentally determined and JCPDS *d* values

	$d_{experiment}$ (Å)	Possible plane	d_{JCPDS} (Å)	Δ (%)
d_1	2.857	(008)	2.878	−0.73
d_2	2.681	(107)	2.765	−3.04
d_3	5.739	(004)	5.753	−0.24
d_4	5.499	(004)	5.753	−4.42

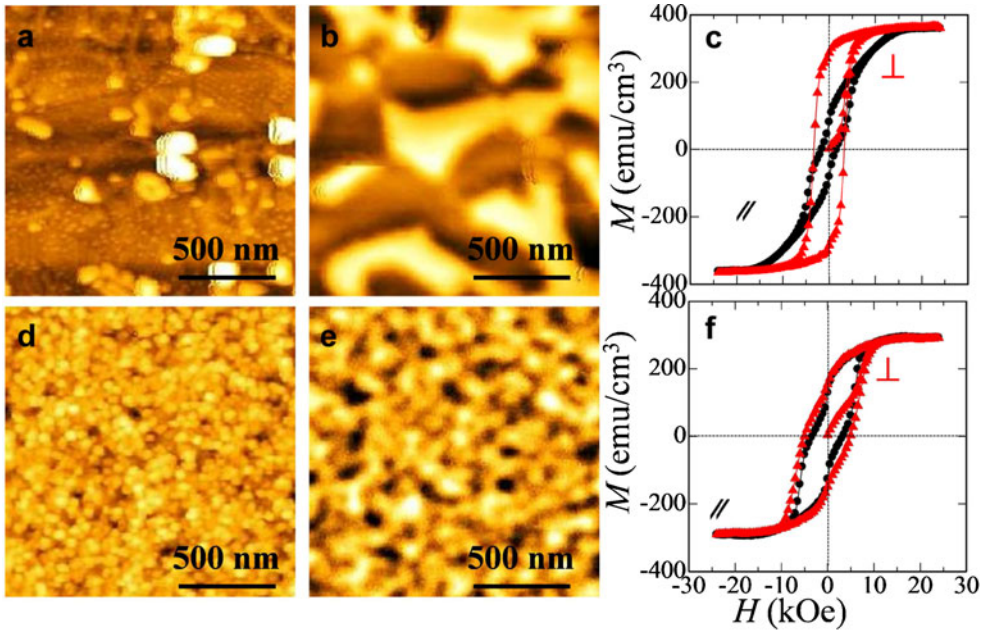

Fig. 5 Nanostructures and magnetic properties of the $SrFe_{12}O_{19}$ (**a**–**c**) and $SrFe_{12}O_{19}$/Au (**d**–**f**) samples shown in Fig. 2e and f and Fig. 2g and h, respectively. **a** and **d** are AFM images, while **b** and **e** are the corresponding MFM images. The magnetic hysteresis loops of both samples are shown in **c** and **f**. Two different directions of magnetic field were applied to the samples, i.e., perpendicular (⊥) to the sample surface and parallel (//) in relation to the sample surface, respectively

downsizing of the $SrFe_{12}O_{19}$ film to form the self-assembled structures was demonstrated by using the self-assembled Au nanoparticle underlayers. The Au nanoparticles are presumed to hinder the continuous growth of $SrFe_{12}O_{19}$ grains. Figure 5b and e show the magnetic domain structures of both samples (the observation areas for Fig. 5b and e are the same as those in Fig. 5a and d, respectively). The bright and dark contrasts indicate the direction of the perpendicular magnetization components of the magnetic domains. That is, perpendicularly upward or downward. Microscale magnetic domains with various shapes were found in $SrFe_{12}O_{19}$ (Fig. 5b), while nanoscale magnetic domains were seen in $SrFe_{12}O_{19}$/Au (Fig. 5e). By comparing the AFM and MFM images, a single $SrFe_{12}O_{19}$ nanomagnetic domain (Fig. 5e) was determined to be slightly larger than a single $SrFe_{12}O_{19}$ nanodot (Fig. 5d). However, it is possible that the resolution of the MFM image is lower than that of the AFM image, because the MFM measurements detect the leakage magnetic fields from the sample surface. Thus, equivalent discussions should not be made regarding the sizes of the magnetic domains and nanodots. The downsizing of the magnetic domains to the nanoscale was actualized through the downsizing of the $SrFe_{12}O_{19}$ grains.

The magnetic hysteresis loops of both samples were acquired at room temperature (Fig. 5c and f). Judging from the magnetic behavior, it was concluded that the $SrFe_{12}O_{19}$ monolayer exhibits perpendicular magnetic anisotropy. The (00*l*) crystallographic orientation of $SrFe_{12}O_{19}$ is essential for perpendicular magnetic anisotropy. In the case of $SrFe_{12}O_{19}$/Au sample, however, isotropic magnetic behavior contributed from out-of-plane and in-plane magnetization components was observed. This result suggests an imperfection in the (00*l*) orientation of $SrFe_{12}O_{19}$ in $SrFe_{12}O_{19}$/Au, which could be attributed to the fluctuation of Au orientation. From Fig. 1c, there might be a trace of Au (200) in the vicinity of $2\theta=44°$, while the existence of Au (200) was not clear from Fig. 4b. The magnetic characteristics for $SrFe_{12}O_{19}$ and $SrFe_{12}O_{19}$/Au did not agree with the results of the TEM and XRD studies. This issue is still an open question in the present study. The saturation magnetization (M_S) value of the $SrFe_{12}O_{19}$ sample was 360 emu/cm^3, which is comparable to that for bulk $SrFe_{12}O_{19}$ [25]. For the $SrFe_{12}O_{19}$/Au sample, the M_S value was smaller than that of the $SrFe_{12}O_{19}$ at 290 emu/cm^3. The reduction of the M_S value for $SrFe_{12}O_{19}$/Au is believed to be reasonable, because the volume fraction of crystalline $SrFe_{12}O_{19}$ in the $SrFe_{12}O_{19}$/Au sample is smaller than that in the $SrFe_{12}O_{19}$ monolayer due to the coexistence of crystalline $SrFe_{12}O_{19}$ and amorphous Sr–Fe–O. Nanofabricated magnetic materials usually show a suppression of magnetic properties attributed to the thermal fluctuations of the small magnetic crystallites; however, serious deterioration of the magnetic characteristics of the $SrFe_{12}O_{19}$ nanodots in $SrFe_{12}O_{19}$/Au was suppressed exhibiting a tolerable magnitude of magnetization, even after nanostructuring of $SrFe_{12}O_{19}$. Furthermore, the magnetic reversal behaviors are discussed herein. An abrupt magnetic reversal was observed in the $SrFe_{12}O_{19}$ sample with a perpendicular coercivity value of 3.4 kOe (Fig. 5c), while the hysteresis loops exhibited gradual slope in the $SrFe_{12}O_{19}$/Au sample (Fig. 5f). The perpendicular coercivity of $SrFe_{12}O_{19}$/Au was 4.7 kOe. We consider that the gradual magnetic switching and increase in the coercivity of $SrFe_{12}O_{19}$/Au sample can be attributed to two reasons; (1) the coexistence of magnetic $SrFe_{12}O_{19}$ and nonmagnetic Sr–Fe–O sections in the same phase and (2) variations in the magnetic anisotropy direction (*c*-axis direction) of $SrFe_{12}O_{19}$

grains. Because the isotropic magnetic hysteresis loops indicated the existence of various anisotropy directions of $SrFe_{12}O_{19}$. In the case of (1), the strength of the intergranular interaction between the magnetic $SrFe_{12}O_{19}$ grains is weaker than that of $SrFe_{12}O_{19}$ monolayer, because the magnetic $SrFe_{12}O_{19}$ grains are separated by the nonmagnetic Sr–Fe–O amorphous sections (Fig. 3a–g). As a result, each $SrFe_{12}O_{19}$ grain independently behaves as an isolated grain. The coercivity value could be different from grain to grain, such that the magnetization of each $SrFe_{12}O_{19}$ grain reverses at various strengths of magnetic field. Therefore, the overall magnetic reversal occurred gradually and overall perpendicular coercivity increased. Concerning (2), the magnetizations of $SrFe_{12}O_{19}$ grains reverse in a wide range of magnetic fields due to the fluctuations of magnetic anisotropy direction. Based on the considerations (1) and (2), the gradual magnetic switching behaviors and increase in the perpendicular coercivity were generated.

The next subject in our study is more precise control of $SrFe_{12}O_{19}$ nanodot intervals. It is essential to control the order of the self-assembled Au nanoparticles used as the underlayer. On the basis of our primary experiments, RF magnetron sputtering with in situ heating of the substrate at a moderate temperature was effective to improve the periodicities of the Au nanoparticles. The size of the Au nanoparticles was also markedly reduced to as small as ≤4 nm. Such Au nanoparticle underlayers will enable the formation of precisely ordered $SrFe_{12}O_{19}$ nanodots at the ~10-nm level.

Conclusions

Spontaneously organized $SrFe_{12}O_{19}$ nanodot structures with a size of 40–50 nm were obtained via plasma-aided nanofabrication. In the present study, the self-assembled Au nanoparticles with the areal density as high as $\sim 1.2 \times 10^{12}$ particles/in. were utilized as underlayers for $SrFe_{12}O_{19}$ and played the role of a template. The site-preferential crystallization of $SrFe_{12}O_{19}$ on the Au nanoparticles was experimentally confirmed. The downsizing of the magnetic domains to the nanometer level was evidenced along with the downsizing of the $SrFe_{12}O_{19}$ grains, preserving the magnetic properties by using the Au nanoparticle underlayers. The effects of the Au nanoparticle underlayers can be summarized as (1) acceleration of the crystallization of $SrFe_{12}O_{19}$, (2) nanoscaling of $SrFe_{12}O_{19}$, and (3) a tendency to improve the (00*l*) orientation of $SrFe_{12}O_{19}$, although this effect cannot be perfectly concluded.

The current fabricated area of the $SrFe_{12}O_{19}$ nanodots is ~8.5 cm^2, which is much larger than that obtained using conventional lithography. The self-assembled $SrFe_{12}O_{19}$ nanostructures were obtained using a simple sputtering method, such that the present technique has significant potential for the manufacture of magnetic nanodots. In the future, we expect to realize a patterned magnetic recording $SrFe_{12}O_{19}$ medium consisting of coexisting nanocrystalline $SrFe_{12}O_{19}$ (magnetic) regions and nanoamorphous Sr–Fe–O (nonmagnetic) regions in the same phase at regular nanointervals.

Acknowledgment This work was financially supported by a Grant-in-Aid for Young Scientists (B) No. 23760280 from the Japan Society for the Promotion of Science (JSPS).

References

1. Perigo EA, Silva SC, de Sousa EMB, Freitas AA, Cohen R, Nagamine LCCM, Takiishi H, Landgraf FJG (2012) Properties of nanoparticles prepared from NdFeB-based compound for magnetic hyperthermia application. Nanotechnol 23:175704/1–175704/10
2. Anirudhan TS, Sandeep S (2012) Synthesis, characterization, cellular uptake and cytotoxicity of a multi-functional magnetic nanocomposite for the targeted delivery and controlled release of doxorubicin to cancer cells. J Mater Chem 22:12888–12899
3. Mink JE, Rojas JP, Logan BE, Hussain MM (2012) Vertically grown multiwalled carbon nanotube anode and nickel silicide integrated high performance microsized (1.25 μL) microbial fuel cell. Nano Lett 12:791–795
4. Asghar G, Nasir S, Awan MS, Tariq GH, Anis-ur-Rehman M (2012) Anomalous behavior of chemically synthesized magnetoplumbite strontium ferrite nano particles. Key Eng Mater 510–511:330–334
5. Lambert SE, Sanders IL, Patlach AM, Krounbi MT, Hetzler SR (1991) Beyond discrete tracks: other aspects of patterned media. J Appl Phys 69:4724–4726
6. Hellwig O, Bosworth JK, Dobisz E, Kercher D, Hauet T, Zeltzer G, Risner-Jamtgaard JD, Yaney D, Ruiz R (2010) Bit patterned media based on block copolymer directed assembly with narrow magnetic switching field distribution. Appl Phys Lett 96:052511/1–052511/3
7. Grobis MK, Hellwig O, Hauet T, Dobisz E, Albrecht TR (2011) High-density bit patterned media: magnetic design and recording performances. IEEE Trans Magn 47:6–10
8. Chikazumi S, Ohta K, Adachi K, Tsuya N, Ishikawa Y (2006) Handbook for magnetic materials. Asakurashoten, Tokyo (in Japanese)
9. Dong Q, Li G, Ho CL, Faisal M, Leung CW, Pong PWT, Liu K, Tang BZ, Manners I, Wong WY (2012) A polyferroplatinyne precursor for the rapid fabrication of $L1_0$-FePt-type bit patterned media by nanoimprint lithography. Adv Mater 24:1034–1040
10. Schmid GM, Miller M, Brooks C, Khusnatdinov N, La Brake D, Resnick DJ, Sreenivasan SV, Gauzner G, Lee K, Kuo D, Weller D, Yang XM (2009) Step and flash imprint lithography for manufacturing patterned media. J Vac Sci Technol B 27:573–580
11. Yang XM, Xu Y, Seiler C, Wan L, Xiao S (2008) Toward 1 Tdot/in.^{2} nanoimprint lithography for magnetic patterned media: opportunities and challenges. J Vac Sci Technol B 26:2604–2610
12. Chappert C, Bernas H, Ferré J, Kottler V, Jamet JP, Chen Y, Cambril E, Devolder T, Rousseaux F, Mathet V, Launois H (1998) Planar patterned magnetic media obtained by ion irradiation. Science 280:1919–1922

13. Suharyadi E, Oshima D, Kato T, Iwata S (2011) Switching field distribution of planar-patterned $CrPt_3$ nanodots fabricated by ion irradiation. J Appl Phys 109:07B771/1–07B771/3
14. Rettner CT, Best ME, Terris BD (2001) Patterning of granular magnetic media with a focused ion beam to produce single-domain islands at >140 Gbit/in^2. IEEE Trans Magn 37:1649–1651
15. Adam JP, Jamet JP, Ferre J, Mougin A, Rohart S, Weil R, Bourhis E, Gierak J (2010) Magnetization reversal in Pt/Co(0.5 nm)/Pt nano-platelets patterned by focused ion beam lithography. Nanotechnol 21:445302/1–445302/5
16. Yang JKW, Chen Y, Huang T, Duan H, Thiyagarajah N, Hui HK, Leong SH, Ng V (2011) Fabrication and characterization of bit-patterned media beyond 1.5 Tbit/in^2. Nanotechnol 22:385301/1–385301/6
17. Sohn JS, Lee D, Cho E, Kim HS, Lee BK, Lee MB, Suh SJ (2009) The fabrication of Co–Pt electro-deposited bit patterned media with nanoimprint lithography. Nanotechnol 20:025302/1–025302/5
18. Zhou Q, Heard PJ, Schwarzacher W (2011) Fabrication and magnetic properties of patterned NiFeMo films electrodeposited in self-assembled nanosphere templates. J Appl Phys 109:054313/1–054313/4
19. Albrecht M, Makarov D (2012) Magnetic films on nanoparticle arrays. Open Surf Sci J 4:42–54
20. Kaewrawang A, Ishida G, Liu X, Morisako A (2008) Epitaxial growth of SrM(00*l*) film on Au(111). IEEE Trans Magn 44:2899–2902
21. Kaewrawang A, Ghasemi A, Liu X, Morisako A (2010) Fabrication, crystallographic and magnetic properties of SrM perpendicular films on Au nanoparticle arrays. J Alloys Compd 492:44–47
22. Kaewrawang A, Ghasemi A, Liu X, Morisako A (2010) Self-assembled strontium ferrite dot array on Au underlayer. J Magn Magn Mater 322:2043–2046
23. Kaewrawang A, Ghasemi A, Liu X, Morisako A (2010) A simple method toward high density SrM dot arrays. J Magn Soc Jpn 34:277–280
24. Yoshida S (1990) Thin films. Baifukan, Tokyo (in Japanese)
25. Ramamurthy Acharya B, Krishnan R, Prasad S, Venkataramani N, Ajan A, Shringi SN (1994) Sputter deposited strontium ferrite films with *c*-axis oriented normal to the film plane. Appl Phys Lett 64:1579–1581